Open access • Journal Article • DOI:10.1007/S10596-007-9071-9

Multiscale finite-volume method for density-driven flow in porous media

Ivan Lunati, Patrick Jenny

Institutions: ETH Zurich

Published on: 15 Jan 2008 - Computational Geosciences (Springer Netherlands)

Topics: Basis function, Multiphase flow, Finite volume method, Flow (mathematics) and Function (mathematics)

Multiscale finite-volume method for density-driven flow in porous media

Originally published in:
Computational Geosciences 12(3), https://doi.org/10.1007/s10596-007-9071-9

Comput Geosci (2008) 12:337–350
DOI 10.1007/s10596-007-9071-9

ORIGINAL PAPER

Multiscale finite-volume method for density-driven flow in porous media

Ivan Lunati · Patrick Jenny

Received: 30 March 2006 / Accepted: 22 August 2007 / Published online: 15 January 2008

Abstract The multiscale finite-volume (MSFV) method has been developed to solve multiphase flow problems on large and highly heterogeneous domains efficiently. It employs an auxiliary coarse grid, together with its dual, to define and solve a coarse-scale pressure problem. A set of basis functions, which are local solutions on dual cells, is used to interpolate the coarse-grid pressure and obtain an approximate fine-scale pressure distribution. However, if flow takes place in presence of gravity (or capillarity), the basis functions are not good interpolators. To treat this case correctly, a correction function is added to the basis function interpolated pressure. This function, which is similar to a supplementary basis function independent of the coarse-scale pressure, allows for a very accurate fine-scale approximation. In the coarse-scale pressure equation, it appears as an additional source term and can be regarded as a local correction to the coarse-scale operator: It modifies the fluxes across the coarse-cell interfaces defined by the basis functions. Given the closure assumption that localizes the pressure problem in a dual cell, the derivation of the local problem that defines the correction function is exact, and no additional hypothesis is needed. Therefore, as in the original MSFV method, the only closure approximation is the localization assumption. The numerical experiments performed for density-driven flow problems (counter-current flow and lock exchange) demonstrate excellent agreement between the MSFV solutions and the corresponding fine-scale reference solutions.

Keywords Gravity · Counter-current flow · Lock-exchange problem · Multiscale methods · Finite-volume methods · Multiphase flow in porous media · Reservoir simulation

This project was supported by the Chevron/Schlumberger Intersect Alliance Technology.

I. Lunati (✉)
Laboratory of Environmental Fluid Mechanics,
EPF Lausanne GR A0 455, Station 2,
CH-1015 Lausanne, Switzerland
e-mail: ivan.lunati@epfl.ch

P. Jenny
Institute of Fluid Dynamics, ETH, Zurich, Switzerland

1 Introduction

Modeling flow and transport in geological porous media is of great importance for practical applications, such as sustainable management of water resources, optimal exploitation of hydrocarbon reservoirs, risk assessment of hazardous waste repositories, or geological sequestration of carbon dioxide. Common to all these problems is the necessity of dealing with large highly heterogeneous formations that exhibit a hierarchy of heterogeneity scales, such as aquifers and reservoirs. A full description of all these scales is computationally expensive and may even exceed current computational capabilities.

To overcome these difficulties, a number of upscaling techniques have been developed in the last 30 years to coarsen the simulation grid (see, e.g., [14]). The basic idea is to replace a heterogeneous medium by an equivalent homogeneous medium that adequately describes the large-scale effects of the small-scale heterogeneity. The price paid to reduce the computational costs is the loss of the fine-scale information. Although these

approaches have proved reliable for many practical problems, there is evidence that applications to contaminant transport or multiphase flow may be problematic. In these cases, the fine-scale structure can have a strong effect on flow and transport at much larger scales, which makes fine-scale information essential to obtain a realistic estimate of quantities of practical interest, such as contaminant distribution or oil recovery.

To avoid this loss of information, a flourishing activity in multiscale modeling of aquifers and reservoirs has been developed. In contrast to upscaling, the focus is not simply on capturing the large-scale behavior of the system, but on solving the problem with the original resolution. The goal is to find a compromise between accuracy and efficiency, i.e., to develop algorithms providing solutions that can be compared with the fine-scale solution in terms of accuracy while keeping the computational costs low – ideally comparable with flow-based upscaling methods. In the context of reservoir modeling, three major families of methods have been introduced: the multiscale finite-element method [8], which results in a velocity field that is not conservative in general and poses difficulties for modeling transport; the mixed multiscale finite-element method [1–6], which is conservative but involves more degrees of freedom; and the multiscale finite-volume (MSFV) method [9, 10], which provides a locally conservative velocity field with the same number of degrees of freedom for the global problem as the multiscale finite-element method.

The MSFV method employs an auxiliary coarse grid, together with its dual, to define and solve a coarse-scale pressure problem. A set of basis functions, which are local solutions on dual cells, is used to interpolate the coarse-grid pressure and obtain an approximate fine-scale pressure distribution. In contrast to other multiscale methods, it has the advantage of being based on the solution of mass-balance equations, which guarantees conservative velocity fields and makes it easier to incorporate additional physics. After having recently modified the MSFV algorithm to model compressible flow [12], in this paper, we continue the effort of adapting the MSFV method to deal with problems involving complex physical processes. In the following, we present an explicit analytical treatment of gravity and capillary forces, and we numerically test the algorithm for density-driven flow problems, i.e., counter-current flow due to buoyancy effects and recirculation induced by density gradients. The main problem here is that these forces cannot be easily included in the basis functions, as they do not scale with the coarse pressure. Moreover, gravity effects cannot be naively added to the coarse-pressure equation, because the resulting basis-function interpolation would be inaccurate, which would result in inaccurate fine-scale fluxes. We show that a correct rigorous treatment of gravity and capillarity can be achieved by adding a correction function to the basis-function interpolated pressure.

2 Mathematical model of multiphase flow

We consider the flow of m incompressible phases in a rigid porous medium, such that, for each phase α, we have a mass-balance equation of the form

$$\phi \frac{\partial}{\partial t} S_\alpha + \nabla \cdot \boldsymbol{u}_\alpha + q_\alpha = 0 \qquad \alpha \in [1, m], \tag{1}$$

where ϕ [m^3/m^3] is the porosity of the medium; S_α [m^3/m^3] the phase saturation; q_α [1/s] the source term (positive when extracted); and

$$\boldsymbol{u}_\alpha = -\lambda_\alpha k \left(\nabla p_\alpha - \rho_\alpha \boldsymbol{g}\right), \tag{2}$$

[m/s] the Darcy velocity (volumetric flux per unit area) of the α-phase. As the flow is incompressible and the porosity constant, in the following, the terms "velocity" and "flux" will be used synonymously. In Eq. 2, $\lambda_\alpha = k_{r\alpha}/\mu_\alpha$ [m s/kg] is the α-phase relative mobility, i.e., the ratio of relative permeability, $k_{r\alpha} \in [0, 1]$, to dynamic viscosity, μ_α (kg/m s); k (m^2) is the intrinsic permeability, which is fluid independent; $\boldsymbol{g}$ (m/s^2) the gravity acceleration vector; p_α (kg/ms^2) and ρ_α (kg/m^3) the pressure and the density of the α-phase, respectively.

The m mass-balance equations can be manipulated to obtain an equation for the pressure of a reference phase ω, $p = p_\omega$, and $m - 1$ transport equations for the saturations, $\boldsymbol{S} = (S_1, S_2, ..., S_{m-1})$. Indeed, defining the macroscopic capillary pressure of the α-phase with respect to the ω-phase,

$$p_{c\alpha\omega} = p_\alpha - p_\omega, \tag{3}$$

and introducing the constitutive relationships, $k_{r\alpha}(\boldsymbol{S})$ and $p_{c\alpha\omega}(\boldsymbol{S})$, and the constraint

$$\sum_{\alpha=1}^{m} S_\alpha = 1, \tag{4}$$

a complete system of equations in the variables p and $\boldsymbol{S}$ is obtained. The pressures of the other phases, $p_{\alpha\neq\omega}$, and the saturation of the m-th phase, S_m, can be obtained from Eqs. 3 and 4, respectively. The pressure equation has the form

$$\nabla \cdot \boldsymbol{u} + q = 0, \tag{5}$$

where we have defined the total velocity, $\boldsymbol{u} = \sum_{\alpha=1}^{m} \boldsymbol{u}_\alpha$, which can be written as

$$\boldsymbol{u} = -\lambda k \left(\nabla p + \boldsymbol{P}_c - \boldsymbol{G}\right). \tag{6}$$

In Eq. 5, $\lambda = \sum_{\alpha=1}^{m} \lambda_\alpha$ is the total mobility;

$$\boldsymbol{G} = \sum f_\alpha \rho_\alpha \boldsymbol{g}, \tag{7}$$

(kg/s^2 m^2) the modified gravity, which represents the gravity force per unit volume acting on the phase mixture;

$$\boldsymbol{P}_c = \sum f_\alpha \nabla p_{c\alpha\omega}, \tag{8}$$

(kg/s^{2}m^2) the modified capillary force per unit volume; and $f_\alpha = \lambda_\alpha/\lambda$ (−) the fractional flow function of the α-phase. Once Eq. 5 is solved for pressure, the velocities of $m-1$ phases can be computed from Eq. 2 or, in a fractional flow formulation, as

$$\boldsymbol{u}_\alpha = f_\alpha \left\{ \boldsymbol{u} + \lambda k \sum_{\beta=1}^{m} f_\beta \left[\nabla \left(p_{c\beta\omega} - p_{c\alpha\omega} \right) - \boldsymbol{g} \left(\rho_\beta - \rho_\alpha \right) \right] \right\}. \tag{9}$$

The phase velocities are then used in the corresponding $m-1$ transport equations, which have the form of Eq. 1. Mass conservation is guaranteed by the constraint $\sum_{\alpha=0}^{m} f_\alpha = 1$.

3 Multiscale finite-volume method

The MSFV method was developed to solve elliptic (homogeneous) equations on large and highly heterogeneous domains efficiently [9]. An auxiliary coarse grid is imposed and, together with its dual, used to define and solve a coarse-pressure problem. The MSFV method employs a set of basis functions, which are local solutions of the elliptic homogeneous equation, to relate the coarse-grid pressure to the fine-scale pressure distribution. The MSFV method has been applied for multiphase-flow problems with simplified physics, i.e., incompressible flow with negligible gravity and capillary effects [10]. In the multiphase-flow framework, the main ideas of the MSFV method deal with the solution of the elliptic pressure equation (5), whereas the phase-transport equations (1) are solved by a standard Schwartz overlap method, which is very efficient for hyperbolic problems and matches the block-based data structure of the MSFV algorithm. As mobility depends on saturation, the basis functions have to be updated. To keep the MSFV method efficient, the basis functions are updated adaptively, i.e., only in regions where mobility changes exceed a specified threshold [10]). This allows reusing most basis functions for the successive step.

Recently, the MSFV method has been modified to provide a suitable framework to describe additional physical processes. This modification has been applied to solve the parabolic pressure equation arising in the case of compressible flow [12]. The modified algorithm consists of three main steps: computation of an approximate pressure solution, which includes the computation of the basis functions to extract effective coarse-scale transmissibilities and the solution of the coarse-scale pressure equation; construction of conservative fine-scale fluxes; and solution of the transport equations. The pressure approximation is defined by means of the dual grid and consists of a juxtaposition of local solutions computed on the dual cells. The flux approximation is defined as a juxtaposition of local solutions computed on the coarse cells with appropriate boundary conditions that guarantee mass conservation. The most important difference compared to the original MSFV method is that the modified algorithm does not use a second set of basis functions to construct the fine-scale fluxes, but solves local problems with full physics. In this framework, the effects of gravity (and capillarity) can be easily included in the fine-scale flux construction, whereas a correction function has to be introduced to obtain an accurate pressure approximation.

4 Pressure approximation

4.1 Finite-volume discretization scheme

The cell-centered finite-volume discretization scheme for the homogeneous elliptic equation,

$$\nabla \cdot \lambda k \nabla p = 0, \tag{10}$$

can be derived as a special case of the more general weighted residual method, which is based on a weak integral form of the differential equation, i.e., $\int_\Omega w \nabla \cdot \lambda k \nabla p \; \mathrm{d}\boldsymbol{x} = 0$. Depending on the choice of the test functions, w, and on the approximation of p, different discretization schemes can be derived (finite-volume, standard finite-elements, etc.).

Let us consider a grid with M nodes and N cells, which defines a partition of the domain, Ω, into N control volumes, $\Omega_i \subset \Omega$. To derive a set of discrete mass-conservation equations, we integrate Eq. 10 over Ω_i, which corresponds to $w(\boldsymbol{x}) = 1$ if $\boldsymbol{x} \in \Omega_i$ and $w(\boldsymbol{x}) = 0$ elsewhere. Applying the Gauss' theorem (or divergence theorem), for the cell Ω_i we obtain

$$\int_{\Omega_i} \nabla \cdot \lambda k \nabla p \; \mathrm{d}\boldsymbol{x} = \int_{\partial\Omega_i} \lambda k \nabla p \cdot \boldsymbol{\eta} \; ds \approx \sum_j T_{ij} \Delta p_{ij} = 0, \tag{11}$$

where $\boldsymbol{\eta}$ is the unit vector orthogonal to $\partial\Omega_i$ pointing outwards. To obtain the discrete transmissibilities, T_{ij}, a choice has to be made to relate the continuous gradient, ∇p, to the discrete potential drop, $\Delta p_{ij} = p_i - p_j$, between the two cells Ω_i and Ω_j. In the standard cell-centered finite-volume method, a piecewise linear interpolation is used and flux continuity is enforced at the interface; in the MSFV method local solutions of the elliptic equation (basis functions) are used as pressure interpolators.

4.2 Basis functions and transmissibilities

The MSFV method employs an auxiliary coarse grid, together with its dual, to solve Eq. 10. Given the domain Ω, a coarse grid with M nodes and N cells is constructed, which defines a partition, $\Omega_{i\in[1,N]}$. A dual coarse grid is constructed such that each dual coarse cell, $\tilde{\Omega}^{e\in[1,M]}$, contains exactly one node of the coarse grid in its interior. The dual coarse grid has N nodes, $\boldsymbol{x}_{j\in[1,N]}$, exactly one in the interior of each coarse cell (Fig. 1).

The MSFV method relies on the possibility of approximating the fine-scale pressure by a juxtaposition of local solutions of Eq. 10 computed in the dual cells, $\tilde{\Omega}^e$, and on the representation of these solutions as

$$p|_{\tilde{\Omega}_e} = \sum_j \tilde{\varphi}_j^e p_j, \tag{12}$$

where the basis functions, $\tilde{\varphi}_j^e$, are local solutions of the flow problem independent of the parameters p_j.

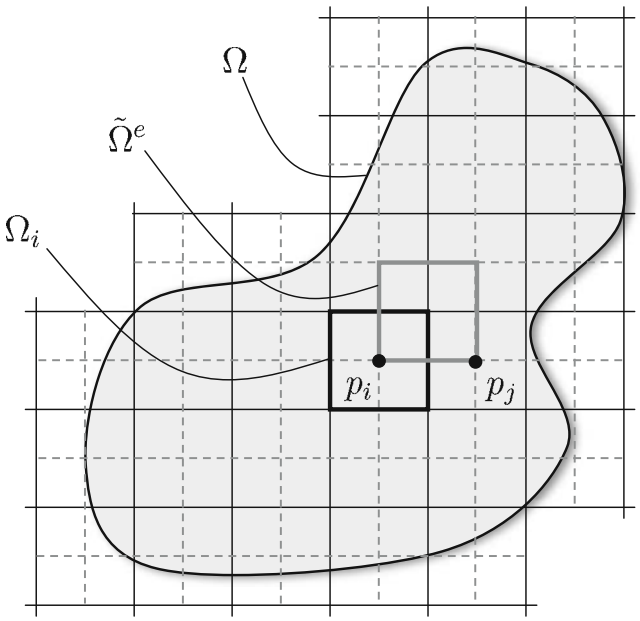

Fig. 1 The coarse grid (*solid line*) together with its dual (*dashed line*)

The accuracy of the method depends on the ability of the boundary conditions assigned on $\partial\tilde{\Omega}^e$ to approximate the actual fine-scale flow conditions.

In the original implementation of the MSFV, it is required that

$$\nabla_\perp \cdot \boldsymbol{u} = 0 \quad \text{on} \quad \partial\tilde{\Omega}^e, \tag{13}$$

where the subscript $\perp$ denotes the projection in the direction normal to $\partial\tilde{\Omega}^e$, i.e., $\nabla_\perp = \boldsymbol{\eta}(\boldsymbol{\eta}\cdot\nabla)$. The use of Eq. 13 to localize the flow problem was first proposed in the multiscale finite-element context [8], and it was demonstrated that it provides accurate MSFV solutions for numerous numerical test cases [9, 10, 12], although some problems may arise for large anisotropy or aspect ratios [13]. As the velocity is divergence free and $\nabla\cdot\boldsymbol{u} = \nabla_\perp\cdot\boldsymbol{u} + \nabla_\parallel\cdot\boldsymbol{u} = 0$, Eq. 13 is equivalent to assigning the solution of the reduced problem $\nabla_\parallel\cdot\boldsymbol{u} = 0$ as Dirichlet boundary conditions on $\partial\tilde{\Omega}^e$. It is further assumed that the parameters, p_j, represent the pressure values at the nodes of the dual grid, $\boldsymbol{x}_{j\in[1,N]}$, i.e.,

$$p(\boldsymbol{x}_j) = p_j, \tag{14}$$

such that the approximate fine-scale pressure is the solution of

$$\begin{cases} \nabla\cdot\lambda k\nabla p = 0 & \text{in} \quad \tilde{\Omega}^e \\ \nabla_\perp\cdot\lambda k\nabla p = 0 & \text{on} \quad \partial\tilde{\Omega}^e \\ p(\boldsymbol{x}_i) = p_i \end{cases}. \tag{15}$$

As the system (15) has to be satisfied for any value of the nodal pressure and the basis functions are independent of p_j, the latter must be solutions of the local problems

$$\begin{cases} \nabla\cdot\lambda k\nabla\tilde{\varphi}_j^e = 0 & \text{in} \quad \tilde{\Omega}^e \\ \nabla_\perp\cdot\lambda k\nabla\tilde{\varphi}_j^e = 0 & \text{on} \quad \partial\tilde{\Omega}^e \\ \tilde{\varphi}_j^e(\boldsymbol{x}_i) = \delta_{ij} \end{cases}. \tag{16}$$

Note that these basis functions satisfy Lagrange's interpolation condition, $\tilde{\varphi}_j^e(\boldsymbol{x}_i) = \delta_{ij}$, and the mass-conservation constraint, $\sum_j \tilde{\varphi}_j^e = 1$. For cartesian grids, which are considered in the following, we have a set of 2^d basis functions per dual cell, $\tilde{\varphi}^e_{j\in[1,2^d]}$, where d is the number of dimensions.

The coarse-scale pressure equation is derived by integration of the fine-scale equation on the control volumes defined by the coarse-grid cells, Eq. 11, and by using the approximate fine-scale pressure, Eq. 12, to compute the fluxes across the control-volume boundaries, i.e., $\lambda k\nabla p\cdot\boldsymbol{\eta} \approx \sum_j p_j\lambda k\nabla\tilde{\varphi}_j^e\cdot\boldsymbol{\eta}$ on $\partial\Omega_i$.

Thus, a system of N algebraic mass-balance equations is obtained,

$$\sum_{j=1}^{3^d} T_{ij} p_j = 0, \quad i \in [1, N], \tag{17}$$

where

$$T_{ij} = -\sum_{e=1}^{2^d} \int_{\partial\Omega_i \cap \tilde{\Omega}^e} \lambda k \nabla \tilde{\varphi}_j^e \cdot \boldsymbol{\eta} \, \mathrm{d}s \tag{18}$$

is the coarse-scale transmissibility pertinent to the node $\boldsymbol{x}_j$. Equation 18 represents the contribution to the flow across $\partial\Omega_i$ for a unit-pressure signal applied at the node $\boldsymbol{x}_j$. It defines the flux across the boundary extracted from all basis functions computed in dual cells that are adjacent to the node $\boldsymbol{x}_j$ and intersect the interface. Note that this results in a 3^d-point stencil and that from the property $\sum_j \tilde{\varphi}_j^e = 1$ directly follow that $T_{ii} = -\sum_{j \neq i} T_{ij}$.

4.3 Local correction to the coarse-scale operator

If the flow of m incompressible phases in presence of gravity and capillary forces is considered, the pressure equation takes the form

$$\nabla \cdot \lambda k \left(\nabla p + \boldsymbol{P}_c - \boldsymbol{G} \right) = 0, \tag{19}$$

and can be regarded as an inhomogeneous elliptic equation in the variable p with source term $-\nabla \cdot \lambda k \left(\boldsymbol{P}_c - \boldsymbol{G} \right)$. If the pressure equation is not homogeneous, the basis functions defined in the previous section are inaccurate pressure interpolators. (The situation here is similar to the one encountered in modeling wells, which has been solved by introducing an additional basis function defined on a well domain [15]). The problem can be easily demonstrated considering a single phase in a heterogeneous medium at hydrostatic conditions. In this case, the pressure is a linearly increasing function of the depth. However, the shape of the basis functions is always dictated by the heterogeneous permeability distribution, and no combination of basis functions exists, which reproduces the correct linear pressure distribution. Therefore, the pressure approximation given by Eq. 12 has to be modified and adapted to the inhomogeneous elliptic problem.

Instead of modifying the basis functions, $\tilde{\varphi}_j^e$, we introduce a local correction function, $\tilde{\varphi}_*^e$, in the definition of the approximate fine-scale pressure, i.e.,

$$p|_{\tilde{\Omega}_e} = \sum_j \tilde{\varphi}_j^e p_j + \tilde{\varphi}_*^e. \tag{20}$$

This correction describes the effects of the inhomogeneous part of the equation. In other words, given the basis functions defined in the previous section, Eq. 16, an appropriate correction function is introduced such that the approximate pressure satisfies the flow problem, Eq. 19, in the dual cell with appropriate boundary conditions, Eq. 13 and Eq. 14. Note that we do not attempt here to improve the boundary conditions used to localize the flow problem. On the contrary, we show how the correction function must be defined such that Eqs. 13 and 14 are still satisfied.

Using Eq. 20, the local problem in a dual cell takes the form

$$\begin{cases} \nabla \cdot \lambda k \left(\sum_j p_j \nabla \tilde{\varphi}_j^e + \nabla \tilde{\varphi}_*^e + \boldsymbol{P}_c - \boldsymbol{G} \right) = 0 & \text{in} \quad \tilde{\Omega}^e \\ \nabla_\perp \cdot \lambda k \left(\sum_j p_j \nabla \tilde{\varphi}_j^e + \nabla \tilde{\varphi}_*^e + \boldsymbol{P}_c - \boldsymbol{G} \right) = 0 & \text{on} \quad \partial\tilde{\Omega}^e \\ \sum_j p_j \tilde{\varphi}_j^e(\boldsymbol{x}_i) + \tilde{\varphi}_*^e(\boldsymbol{x}_i) = p_i \end{cases}, \tag{21}$$

and with the definition of the basis functions, Eq. 16, we obtain the following local problem

$$\begin{cases} \nabla \cdot \lambda k \left(\nabla \tilde{\varphi}_*^e + \boldsymbol{P}_c - \boldsymbol{G} \right) = 0 & \text{in} \quad \tilde{\Omega}^e \\ \nabla_\perp \cdot \lambda k \left(\nabla \tilde{\varphi}_*^e + \boldsymbol{P}_c - \boldsymbol{G} \right) = 0 & \text{on} \quad \partial\tilde{\Omega}^e \\ \tilde{\varphi}_*^e(\boldsymbol{x}_i) = 0 \end{cases}, \tag{22}$$

which defines $\tilde{\varphi}_*^e$. Note that no additional hypothesis has been made: The derivation of Eq. 22 is exact and unique, i.e., no other correction function exists that is consistent with Eqs. 13, 14, and 16.

The coarse-pressure equation can be obtained by integrating the differential equation, Eq. 19, over the coarse cells, Ω_i, and applying Gauss' theorem (or divergence theorem), which yields

$$\int_{\partial\Omega_i} \lambda k \nabla p \cdot \boldsymbol{\eta} \, \mathrm{d}s = -\int_{\partial\Omega_i} \lambda k \left(\boldsymbol{P}_c - \boldsymbol{G} \right) \cdot \boldsymbol{\eta} \, \mathrm{d}s. \tag{23}$$

Using the approximate pressure, Eq. 20, we obtain a set of discrete coarse-scale pressure equations,

$$\sum_{j=1}^{3^d} T_{ij} p_j = \sum_{e=1}^{2^d} \int_{\partial\Omega_i \cap \tilde{\Omega}^e} \lambda k \nabla \tilde{\varphi}_*^e \cdot \boldsymbol{\eta} \, \mathrm{d}s + \int_{\partial\Omega_i} \lambda k \left(\boldsymbol{P}_c - \boldsymbol{G} \right) \cdot \boldsymbol{\eta} \, \mathrm{d}s \quad i \in [1, N], \tag{24}$$

where transmissibilities are still defined by Eq. 18. The terms on the r.h.s. represent two surface source terms on $\partial\Omega_i$. As the coarse-scale operator, T_{ij}, does not include capillary and gravity effects, this operator gives incorrect fluxes across $\partial\Omega_i$ for a given pressure drop between grid nodes. The first term on the r.h.s., which contains $\tilde{\varphi}_*^e$, represents a correction to these inaccurate fluxes and can be regarded as a local correction to the

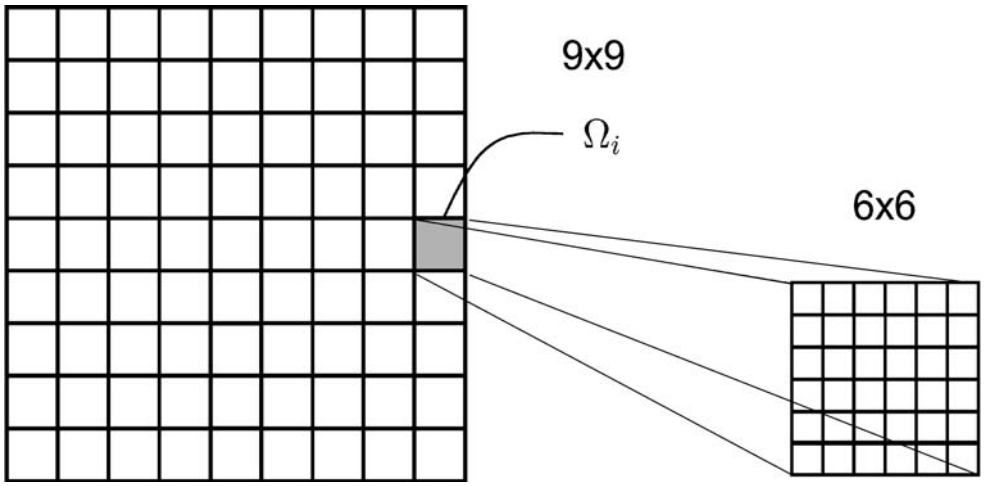

Fig. 2 The coarse grid used for numerical tests consists of 9×9 blocks, Ω_i, each of which contains 6×6 fine cells

coarse-scale operator independent of the coarse-scale pressure.

5 Adaptivity

The computational efficiency of the MSFV method relies on the fact that most basis functions can be reused at successive time steps. To avoid computationally expensive recalculations, an adaptivity criterion based on total-mobility changes has been introduced. Rigorously, the basis functions should be recomputed every time that total mobilities vary in their local support, $\tilde{\Omega}^e$, due to changes in saturation; in practice, they are updated only if the condition

$$\frac{1}{1+\epsilon_\lambda} < \frac{\tilde{\lambda}|_{\tilde{\Omega}^e}}{\lambda|_{\tilde{\Omega}^e}} < 1+\epsilon_\lambda, \tag{25}$$

is violated [10]. In Eq. 25, $\epsilon_\lambda > 0$ is a user-defined threshold, and $\tilde{\lambda}$ is the total mobility used to compute the current basis functions, i.e., the mobility at the last update.

This strategy can be easily extended to problems in which gravity is important. In general, however, the criterion above is not sufficient to guarantee an accurate correction function, as it can be easily understood by considering the case of linear permeabilities and equal viscosities: As $\lambda = 1$ independently of the pressure, Eq. 25 is always satisfied, and the correction function is never updated. The source term in Eq. 22, i.e., $Q = -\nabla \cdot \lambda k(\boldsymbol{P}_c - \boldsymbol{G})$, varies with the saturation and requires the correction function to be recomputed. For this reason, an additional criterion is introduced, i.e.,

$$\frac{1}{1+\epsilon_*} < \frac{\tilde{Q}|_{\tilde{\Omega}^e}}{Q|_{\tilde{\Omega}^e}} < 1+\epsilon_*, \tag{26}$$

where $\epsilon_* > 0$ is a second user-defined threshold and $\tilde{Q}$ is the source term used to compute the current correction function. If Eq. 25 is violated, we set $\tilde{\lambda}|_{\tilde{\Omega}^e} = \lambda|_{\tilde{\Omega}^e}$ and $\tilde{Q}|_{\tilde{\Omega}^e} = Q|_{\tilde{\Omega}^e}$ and recompute all basis functions and the correction function pertinent to the dual cell, $\tilde{\Omega}^e$; if only Eq. 26 is violated, instead, we set $\tilde{Q}|_{\tilde{\Omega}^e} = Q|_{\tilde{\Omega}^e}$ and recompute only the correction function. In the latter case, the total-mobility field used to compute the correction function is not updated, which guarantees that the total-mobility fields used for basis and correction functions are always identical. Note that there is only one correction function per dual cell, hence, only one problem per dual cell has to be solved when only Q changes significantly.

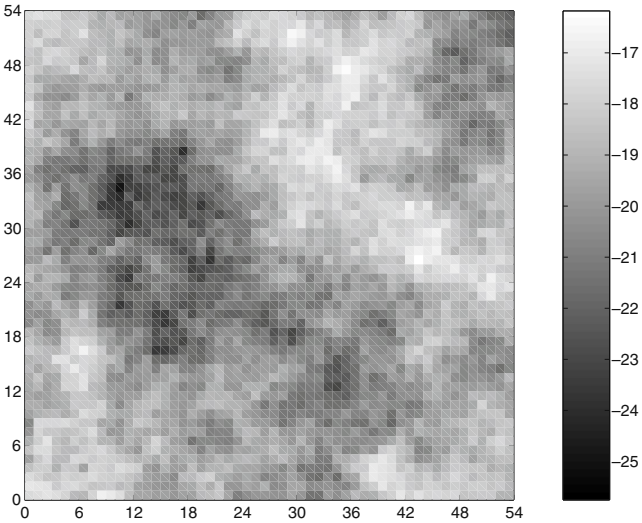

Fig. 3 Natural logarithm of the 2D permeability field. The geometric mean of the permeability is $k_g = 1.3\ 10^{-9}$ m^2; the variance of the log-permeability is $\sigma^2_{\ln k} = 2.52$

Table 1 Phase properties used for the numerical simulations; porosity is $\phi = 0.2$

	μ_α (Pa s)	ρ_α (kg/m^3)	k_α (−)	$p_{c\alpha}$ (Pa)
Water	10^{-3}	1,000	S_α^2	0
Oil	10^{-2}	500	S_α^2	0
Dummy phase	10^{-2}	500	S_α^2	0

6 Flux approximation

The approximate pressure field cannot be used directly to compute the fine-scale fluxes. Indeed, the corresponding fluxes are, in general, discontinuous at the dual-cell interfaces and would lead to severe mass-balance errors [9]. For this reason, the approximate fluxes are constructed as a juxtaposition of fluxes obtained from local pressure solutions of Eq. 19 computed on the coarse cells, Ω_i. The Neuman boundary conditions assigned on $\partial\Omega_i$ are extracted from the approximate pressure solution, Eq. 20, which guarantees local mass conservation. Therefore, the fine-scale total velocity can be written as

$$\boldsymbol{u}|_{\Omega_i} = -\lambda k \nabla(\psi_i + \boldsymbol{P}_c - \boldsymbol{G}), \tag{27}$$

where ψ_i is the solution of the local problem

$$\begin{cases} \nabla \cdot \lambda k \nabla(\psi_i + \boldsymbol{P}_c - \boldsymbol{G}) = 0 & \text{in} \quad \Omega_i \\ \nabla\psi_i \cdot \boldsymbol{\eta} = \nabla\left(\sum_j \tilde{\varphi}_j^e p_j + \tilde{\varphi}_*^e\right) \cdot \boldsymbol{\eta} & \text{on} \quad \partial\Omega_i \cap \tilde{\Omega}^e \end{cases} . \tag{28}$$

7 Phase-transport equations and coupling

Once the approximate total velocity field has been computed, the phase velocity can be obtained from Eq. 9 and used in the fine-scale phase-transport equations. A Schwartz overlap method is applied: The transport problem is solved locally in each coarse volume with boundary conditions from the adjacent cells. Saturation at the boundary is matched by iteration. More precisely, a system of $m-1$ equations of the form

$$\begin{cases} \dfrac{\phi}{\Delta t}\left(S_\alpha^\nu - S_\alpha^n\right) + \nabla \cdot \boldsymbol{u}_\alpha(\boldsymbol{S}^\nu) = 0 & \text{in} \quad \Omega_i \\ \boldsymbol{u}_\alpha(\boldsymbol{S}^{\nu-1}) & \text{on} \quad \partial\Omega_i \end{cases} \tag{29}$$

is solved. The superscripts ν and n denote the current iteration level and the old time step, respectively. In general, the phase velocity is a nonlinear function of saturation, and therefore, the linearization

$$\boldsymbol{u}_\alpha(\boldsymbol{S}^\nu) \approx \boldsymbol{u}_\alpha(\boldsymbol{S}^{\nu-1}) + \sum_{\beta=1}^{m-1} \frac{\mathrm{d}\boldsymbol{u}_\alpha}{\mathrm{d}S_\beta}\bigg|_{\boldsymbol{S}=\boldsymbol{S}^{\nu-1}} \left(S_\beta^\nu - S_\beta^{\nu-1}\right), \tag{30}$$

is used and Eq. 29 is solved by a Newton–Raphson method. The resulting saturation distribution determines a new total mobility field and a new source term for the pressure equation. Coupling between pressure and saturation equations is achieved through a second iteration loop, which yields a sequential fully implicit algorithm [11]. The solution algorithm is outlined below:

Algorithm: *Solution algorithm for flow and transport*

```
n=0
do
  ζ = 0, S^ζ = S^n
  do
    S = S^ζ
    if Eq. 25 is not fulfilled then
      update φ̃^e_{j∈[1,2^d]} and φ̃^e_*        (Eqs. 16 and 22)
    else if Eq. 26 is not fulfilled then
      update φ̃^e_*                            (Eq. 22)
    extract coarse-grid transmissibilities     (Eq. 18)
    solve coarse-grid pressure equation        (Eq. 24)
    construct flux approximation               (Eq. 28)
    ν = 0, S^ν = S
    do
      ν = ν + 1
      solve phase-transport equations          (Eq. 29)
    until max_α |S^ν_α − S^{ν−1}_α|_∞ < ε
    ζ = ζ + 1, S^ζ = S^ν
  until max_α |S^ζ_α − S^{ζ−1}_α|_∞ < ε
  S^{n+1} = S^ζ
  n=n+1
until simulation is done
```

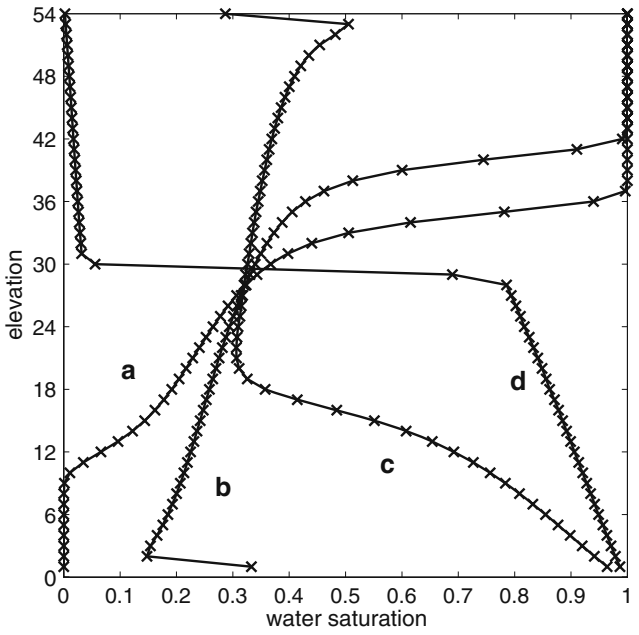

Fig. 4 Counter-current flow in the homogeneous permeability field. Vertical water-saturation profile of the MSFV solution (*crosses*) and fine-scale solution (*solid line*) at dimensionless times **a** 0.16, **b** 0.32, **c** 0.8, and **d** 1.6. The time-step size is 1.6 10^{-2}

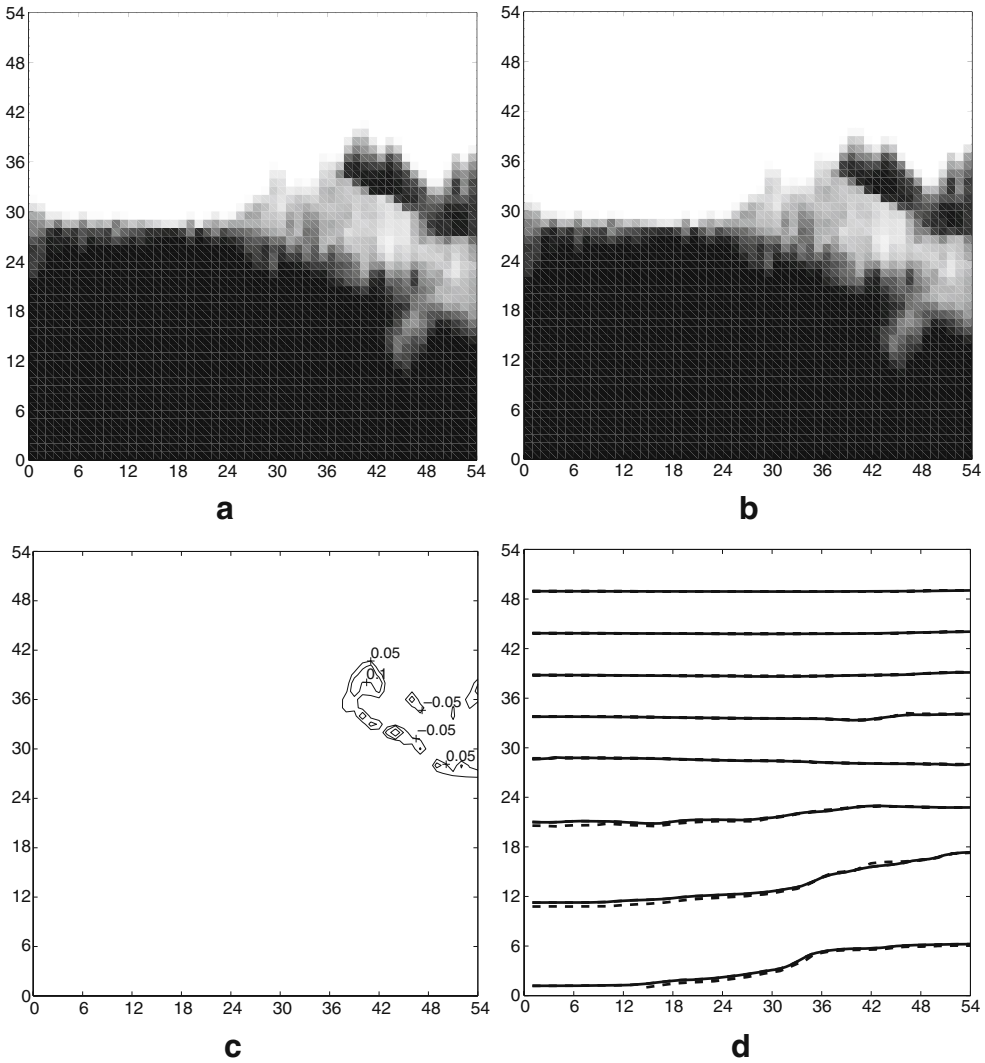

Fig. 5 Counter-current flow in the heterogeneous permeability field. **a** Fine-scale reference solution for saturation (*black* corresponds to $S_w = 0$, *white* to $S_w = 1$); **b** MSFV solution; **c** saturation error, i.e., $\Delta S = S_{\mathrm{MSFV}} - S_{\mathrm{ref}}$, isoline are drawn at $\Delta S = -0.3, -0.1, -0.05, 0.05, 0.1, 0.3$; **d** fine-scale reference solution (*solid line*) and MSFV solution (*dashed line*) for pressure. Shown are the results at dimensionless time 0.2; the time-step size is $2\ 10^{-3}$

8 Numerical results

In this section, the accuracy of the MSFV method for density-driven flow is investigated by comparison with reference solutions obtained solving the same problem on the fine grid. We consider two types of problems: counter-current and lock-exchange flow. The former test deals with a situation in which the different phases can flow in opposite directions and raises mass-balance issues for a three-phase system. However, the total velocity is zero under purely counter-current flow conditions (homogeneous medium with vertical density variations), such that the phase flow is only dictated by local density differences. The lock-exchange problem is more severe, as the horizontal density gradient yields a nonzero total velocity and induces recirculation. Note that, although the flow is purely gravity induced, the phase behavior is determined by the competition between the local gravity effects and the global pressure distribution that is far from being hydrostatic and dictates the total velocity.

The numerical simulations are performed on a 2D discrete domain of size $L \times L$ that is represented on a 54×54 cell fine grid. The coarse grid employed for the MSFV method consists of 9×9 cells (Fig. 2). No-flow boundary conditions apply to all four sides of the domain. Two permeability fields are considered: a homogeneous field with $k = 10^{-9}$ m^2 and a heterogeneous field (Fig. 3), which has been extracted from the top layer of the second model of the SPE10 Comparative Solution Project [7]. The geometric mean of the heterogeneous field is $k = 1.3\ 10^{-9}$ m^2, and the variance of the log-normal permeability is $\sigma^2_{\ln k} = 2.52$.

We consider a three-phase system consisting of water, oil, and a dummy phase, which has the same properties of the oil phase (the parameters used in the simulations are given in Table 1). Capillary forces are neglected. Two transport equations are solved, one for

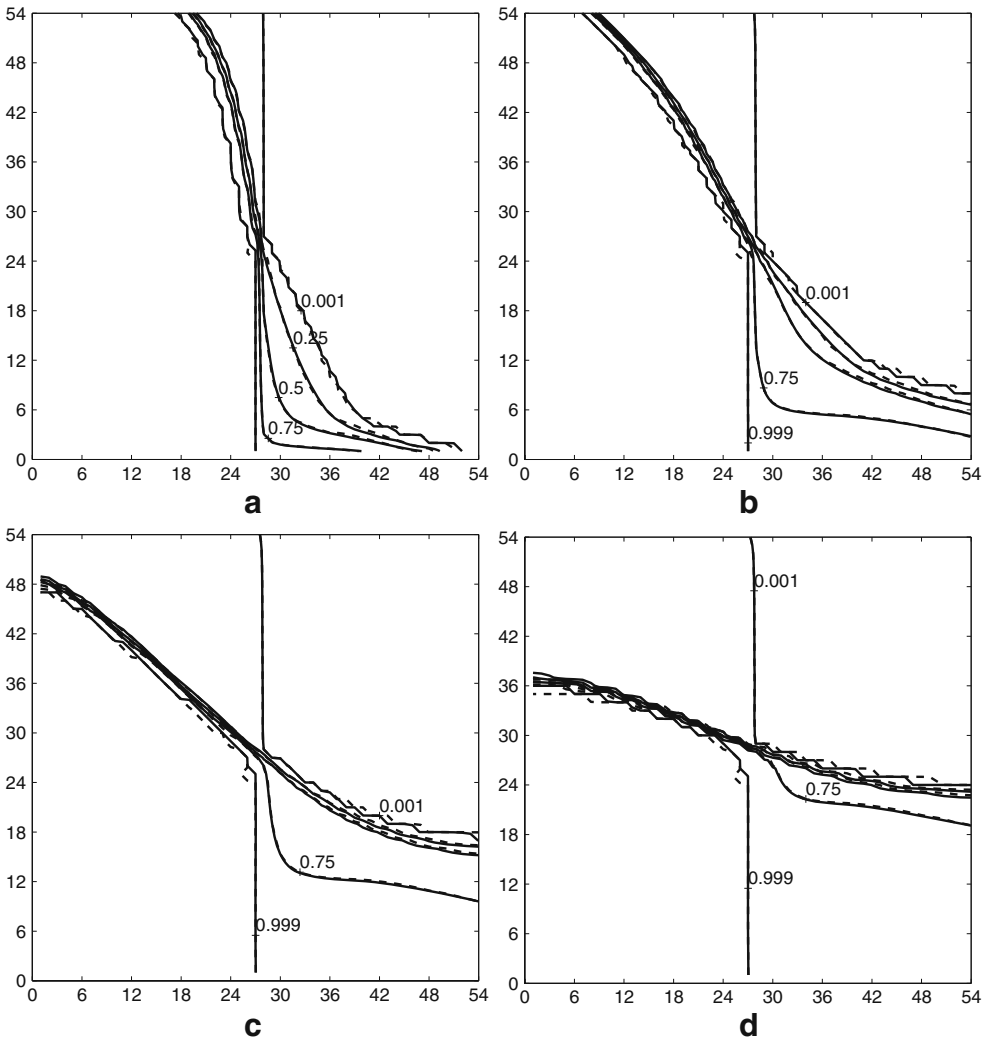

Fig. 6 Lock-exchange problem in the homogeneous permeability field. Water-phase saturation contour lines (0.001, 0.25, 0.50, 0.75, and 0.999) of the fine-scale solution (*solid contours*) and the MSFV solution (*dashed contours*) at dimensionless times **a** 0.08, **b** 0.24, **c** 0.58, and **d** 0.8. The time-step size is 4 10^{-3}

water and one for oil, whereas the saturation of the third phase is obtained from Eq. 4. The saturation of the dummy phase, which is initially zero, is monitored to check material balance. In all the numerical simulations, $\epsilon = 10^{-4}$ is used as convergence criterion; $\epsilon_\lambda = 0.1$ and $\epsilon_* = \infty$ are used for adaptivity. With these thresholds, the correction function is updated only if the basis functions are updated. Typically, less than 20% of the basis functions are recomputed at each time step (2% per iteration loop). Few details about the material-balance error and the selective basis-function update are given in Appendix 1 and the implementation details in Appendix 2.

8.1 Counter-current flow

In the counter-current flow problem, oil initially fills the lower half of the domain, while water occupies the upper part. At time zero, both phases begin to move due to buoyancy effects. The evolution of the vertical water-saturation profile in the homogeneous permeability field is shown in Fig. 4. Note that gravity does not contribute to the total velocity in this case and that the profile is asymmetric due to the relatively large viscosity ratio, $\mu_o/\mu_w = 10$. It can be observed that the MSFV solution and the reference solution are almost identical.

In Fig. 5, the MSFV solution and the reference solution are compared for the heterogeneous permeability field. The results at the dimensionless time $t/\tau = 0.2$ [where $\tau = \phi L(\mu_w + \mu_o)/kg\Delta\rho$] are shown. It can be seen that, also in the heterogeneous case, the MSFV solution is in excellent agreement with the reference.

8.2 Lock-exchange problem

In the lock-exchange problem, water initially occupies the left half of the domain, while oil fills the right part. Due to the density difference, recirculation is

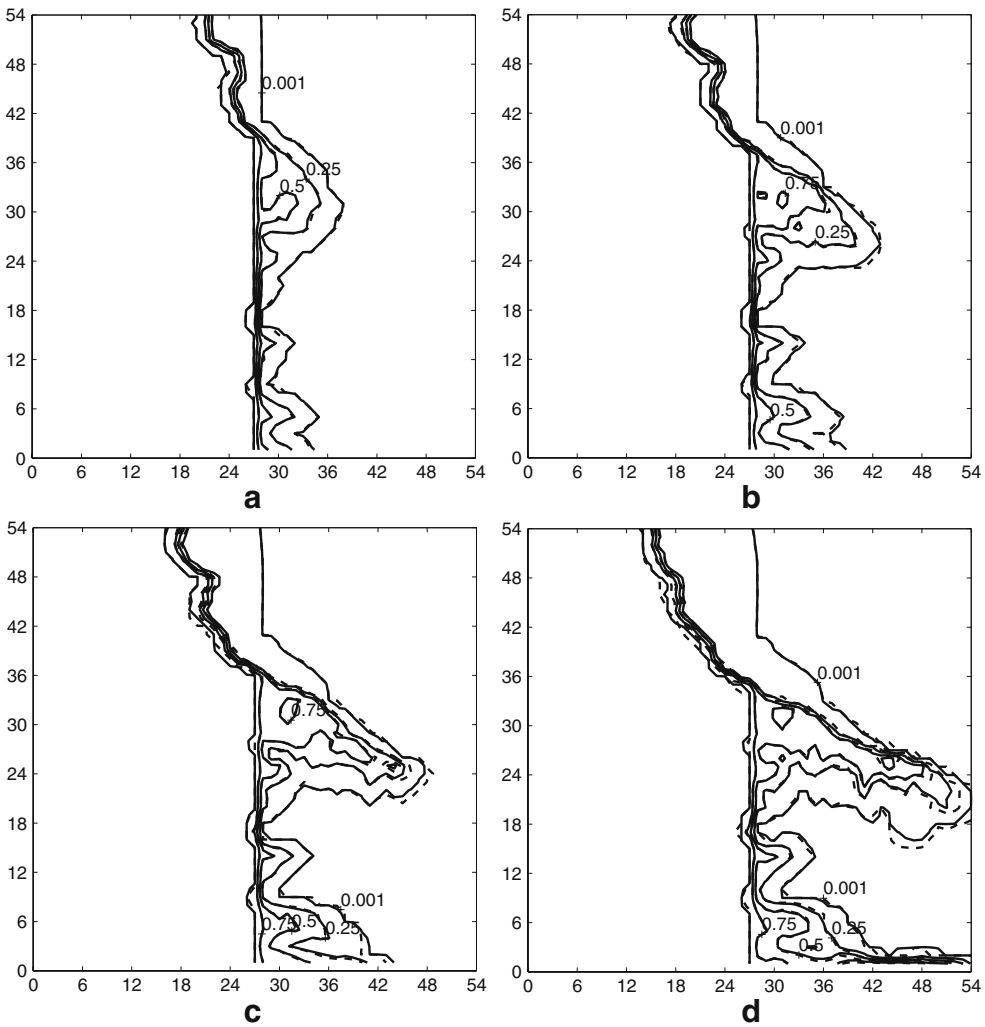

Fig. 7 Lock-exchange problem in the heterogeneous permeability field. Water-phase saturation contour lines (0.001, 0.25, 0.50, 0.75, and 0.999) of the fine-scale solution (*solid contours*) and the MSFV solution (*dashed contours*) at dimensionless times **a** $1.6\ 10^{-2}$, **b** $3.2\ 10^{-2}$, **c** $4.8\ 10^{-2}$, and **d** $8\ 10^{-2}$. The time-step size is $8\ 10^{-4}$

induced. The lock-exchange problem is more challenging because, in contrast to the counter-current flow problem, gravity significantly contributes to the total velocity and localization is more critical. Indeed, an accurate global information about pressure is needed to correctly capture the density-current flow induced in the horizontal direction.

The evolution of the saturation distributions for the homogeneous and the heterogeneous permeability fields is compared in Figs. 6 and 7, respectively. Shown are the water-saturation contour lines for the MSFV solution and the reference solution at four different times. Note the sharp drainage front (oil invasion) and the expansion wave behind the wetting front (water invasion) due to the viscosity difference. The two solutions are in excellent agreement even after large simulation times, which proves that the velocities of the two invading fronts are accurately captured.

Finally, in Fig. 8b, the MSFV pressure is compared with the pressure obtained by superposition of the basis functions without correction, i.e., from Eq. 12. Shown are the results obtained for the heterogeneous permeability field at dimensionless time $t/\tau = 8\ 10^{-2}$. It can be observed that, without correction, the pressure is much more irregular and strongly dictated by the heterogeneity. With the correction function, the pressure becomes smoother, and the agreement with the reference pressure is excellent (Fig. 8a). Note that the correction is zero at the horizontal dual-cell boundaries (Fig. 8d). Indeed, as gravity is perpendicular to these boundaries, the condition at $\partial\tilde{\Omega}^e$ in Eq. 22 is equivalent to a reduced problem without source term, which results in no correction along the horizontal boundaries. Note also that the correction is effective in regions where only one phase is present. This is due to the fact that the basis functions are inaccurate pressure interpolators also for single-phase flow if gravity is not negligible, as discussed at the beginning of Section 4.3 for the hydrostatic solution. Numerical simulations (not presented here) have shown that the approximate

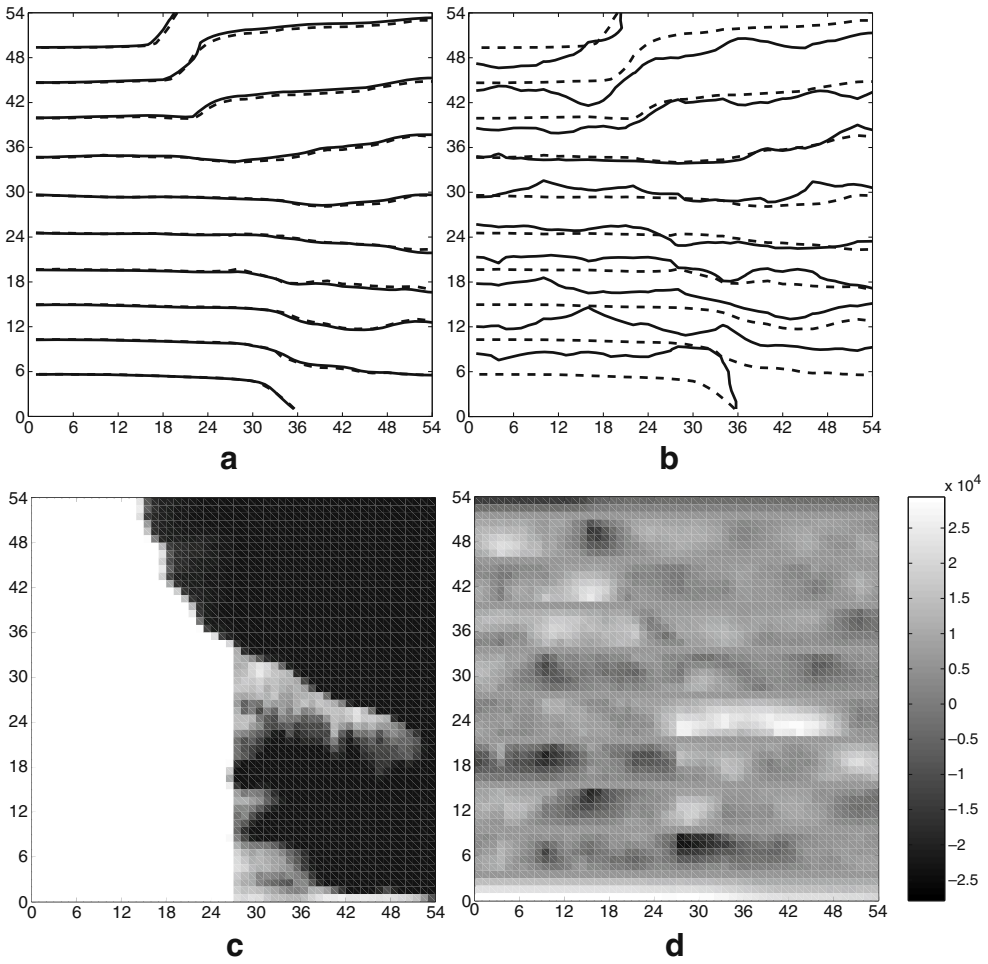

Fig. 8 Lock-exchange problem in the heterogeneous permeability field. **a** Fine-scale reference pressure (*solid line*) and MSFV pressure (*dashed line*); **b** MSFV pressure (*dashed line*) and pressure obtain by superimposition of the basis function without correction (*solid line*); **c** fine-scale solution for saturation (*black* corresponds to $S_w = 0$, *white* to $S_w = 1$); **d** correction function. Shown are the results at dimensionless time $8\ 10^{-2}$; the time-step size is $8\ 10^{-4}$

pressure with correction function can exactly reproduce the hydrostatic pressure solution for single- and multiphase flow in heterogeneous permeability fields.

9 Conclusions

An accurate treatment of density-driven flow in the MSFV method has been achieved by adding a correction function to the basis-function interpolated pressure. This correction, which can be interpreted as a supplementary basis function independent of the coarse-scale pressure, appears in the coarse-grid pressure equation as an additional source term. It can be regarded as a local correction to the coarse-scale operator, which modifies the fluxes between coarse cells generated by the basis-function interpolated pressure. The derivation of the local problem that defines the correction function does not require any additional assumption. As in the original MSFV, the only approximation is the localization of the pressure equation to compute basis and correction functions.

Introducing the correction function yields a very accurate fine-scale pressure field for multiphase flow with gravity. The numerical experiments performed for density-driven flow problems (counter-current flow and lock-exchange) demonstrate that the MSFV solutions for pressure and saturation are in excellent agreement with the corresponding fine-scale reference solutions. This proves that the solution of the reduced problems on the cell boundaries provides a good estimate of the actual fine-scale flow conditions even in presence of gravity. From a computational view point, it is important to observe that basis and correction functions can be updated adaptively, which makes the MSFV method very efficient for large problems.

Similar results are expected for problems with capillary effects, whose treatment in terms of correction function has been presented, but has not been tested numerically. Indeed, capillarity and gravity have similar effects on the structure of the pressure equation, as they both appear as saturation-dependent source terms. The correction function presented here provides a framework that can be generalized for all those cases dealing

with inhomogeneous elliptic equations, e.g., due to the presence of distributed sources or accumulation terms as for compressible flow.

Acknowledgements We thank S. H. Lee, C. Wolfsteiner, and H. A. Tchelepi for many constructive discussions.

Appendix

Appendix 1: Material balance and adaptivity

All numerical simulations are performed for a three phase system. The saturation of the third phase, which is initially zero (dummy phase), is computed as $S_d = 1 - S_w - S_o$ and used to check the material balance. The maximum saturation, $\max_{\boldsymbol{x}\in\Omega}\{S_d(\boldsymbol{x})\}$, and the total mass per unit volume, $\int_\Omega S_d(\boldsymbol{x})\mathrm{d}\boldsymbol{x}/\int_\Omega \mathrm{d}\boldsymbol{x}$, of the reference solution and of the MSFV solution are compared in Fig. 9a and b, respectively. Shown are the solutions of the lock-exchange problem in the homogeneous permeability field. The maximum saturation of the dummy phase reaches a value about ten times larger than the value used for the convergence criterion, $\epsilon = 10^{-4}$. Note that the behaviors of the MSFV solution and the reference solution are quantitatively very similar. Additional numerical simulations (not presented here) have shown that the error can be arbitrarily reduced by reducing ϵ. The other numerical simulations presented in these paper exhibit similar behaviors, the simulations performed in the heterogeneous permeability field showing some fluctuations.

The fraction of update basis and correction functions per time step, F_t, is defined as the number of dual cells in which these functions are updated, M_u, divided by the number of dual cells, M, and it is shown in Fig. 9c. Typically, the basis functions have to be updated in less than 20% of the dual cells. Figure 9d shows the

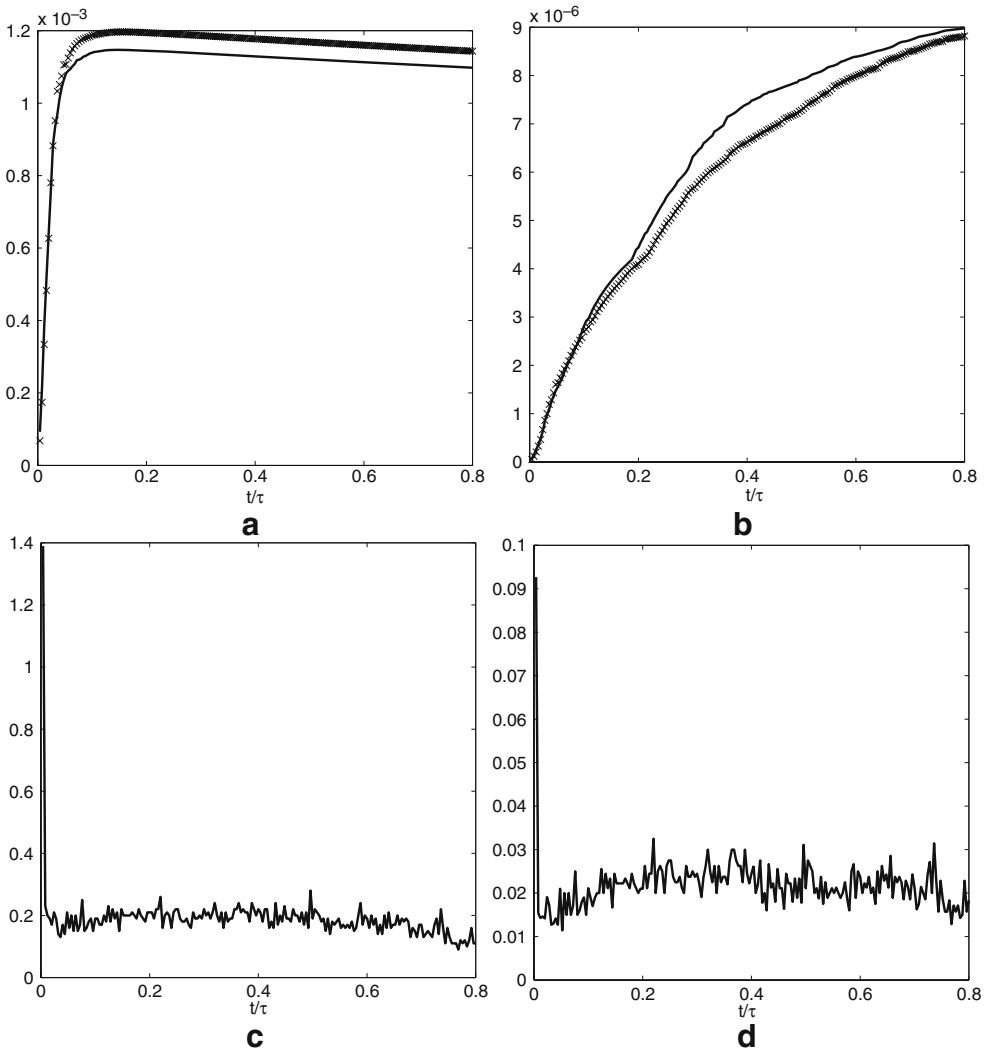

Fig. 9 Lock-exchange problem in the homogeneous permeability field. **a** Maximum saturation of the dummy phase, $\max_{\boldsymbol{x}\in\Omega} S_d$, and **b** total dummy-phase mass per unit volume, $\int_\Omega S_d\mathrm{d}\boldsymbol{x}/\int_\Omega \mathrm{d}\boldsymbol{x}$, for the fine-scale (*solid line*) and the MSFV solutions (*crosses*) as a function of the dimensionless time; fraction of recomputed basis functions per time step (**c**) and per iteration loop (**d**) as a function of dimensionless time

fraction of basis functions update per iteration loop, $F_\zeta = F_t/n_\zeta$, where n_ζ is the number of iterations. The percentage of recomputed basis and correction functions is similar for the other numerical tests performed.

Appendix 2: Implementation details

Throughout the paper, a continuous notation has been employed for problems to be solved at fine scale. In the numerical simulations, however, these problems have been solved on a discrete grid (the original fine-scale grid) with a cell-centered finite-volume method. In this section, we present few details about the discretization used.

2.1 Fine-scale reference solution

Given two fine-scale cells of a cartesian grid, Ω'_i and Ω'_j, the discrete fluxes across the interface $\partial\Omega'_{ij} = \dot{\Omega}'_i \cup \dot{\Omega}'_j$ directed from Ω'_i to Ω'_j can be written in the form $A_{ij}[\mathrm{u}]_{\mathrm{ij}}$, where

$$[\boldsymbol{u}]_{ij} = -[\lambda]^{\mathrm{U}}_{ij}\,[k]^{\mathrm{H}}_{ij}\left\{\frac{p(\boldsymbol{x}_j)-p(\boldsymbol{x}_i)}{|\boldsymbol{x}_j-\boldsymbol{x}_i|} - g_{ij}\sum_{\alpha=1}^{m}[f_\alpha]^{\mathrm{U}}_{ij}\,\rho_\alpha\right\}. \tag{31}$$

is the total velocity evaluated at the interface; A_{ij} is the area of the interface; $\boldsymbol{x}_j$ and $\boldsymbol{x}_i$ the coordinates of the cell centers; and $g_{ij} = \boldsymbol{g}\cdot(\boldsymbol{x}_j-\boldsymbol{x}_i)/|\boldsymbol{x}_j-\boldsymbol{x}_i|$ the component of the gravity perpendicular to the interface. Square brackets, $[\ ]_{ij}$, indicate that the corresponding quantities are evaluated at the interface; the superscripts A and H denote arithmetic and harmonic mean of the corresponding cell quantities, respectively. The superscript U indicates that a phase-by-phase upwind scheme is employed; e.g., for the mobility

$$[\lambda_\alpha(S_\alpha)]^{\mathrm{U}}_{ij} = \lambda_\alpha\left([S_\alpha]^{\mathrm{U}}_{ij}\right) = \begin{cases}\lambda_\alpha(S_i) & \text{if}\quad [\boldsymbol{u}_\alpha]_{ij} > 0\\ \lambda_\alpha(S_j) & \text{if}\quad [\boldsymbol{u}_\alpha]_{ij} < 0\end{cases}. \tag{32}$$

Therefore, we have $[\lambda]^{\mathrm{U}}_{ij} = \sum_{\beta=1}^{m}[\lambda_\beta]^{\mathrm{U}}_{ij}$ and $[f_\alpha]^{\mathrm{U}}_{ij} = [\lambda_\alpha]^{\mathrm{U}}_{ij}/[\lambda]^{\mathrm{U}}_{ij}$, which satisfies the constraint $\sum_{\alpha=1}^{m}[f_\alpha]_{ij} = 1$ and guarantees the conservation of mass.

2.2 MSFV method

When computing basis, $\tilde{\varphi}^e_l$, and correction functions, $\tilde{\varphi}^e_*$, the total velocity at the interface is evaluated as

$$[\boldsymbol{u}]_{ij} = -[\lambda]^{\mathrm{A}}_{ij}\,[k]^{\mathrm{H}}_{ij}\,\frac{\tilde{\varphi}^e_l(\boldsymbol{x}_j)-\tilde{\varphi}^e_l(\boldsymbol{x}_i)}{|\boldsymbol{x}_j-\boldsymbol{x}_i|}, \tag{33}$$

and

$$[\boldsymbol{u}]_{ij} = -[\lambda]^{\mathrm{A}}_{ij}\,[k]^{\mathrm{H}}_{ij}\left\{\frac{\tilde{\varphi}^e_*(\boldsymbol{x}_j)-\tilde{\varphi}^e_*(\boldsymbol{x}_i)}{|\boldsymbol{x}_j-\boldsymbol{x}_i|} - g_{ij}\sum_{\alpha=1}^{m}[f_\alpha]^{\mathrm{A}}_{ij}\,\rho_\alpha\right\}, \tag{34}$$

respectively. Note that a central scheme is used for the phase mobility, such that these functions are independent of the coarse-scale pressure. When computing the approximate fluxes in a coarse cell, Ω_l, the velocity at the interface is evaluated as

$$[\boldsymbol{u}]_{ij} = -[\lambda]^{\mathrm{U}}_{ij}\,[k]^{\mathrm{H}}_{ij}\left\{\left[\frac{\Delta p}{\Delta x}\right]_{ij} - g_{ij}\sum_{\alpha=1}^{m}[f_\alpha]^{\mathrm{U}}_{ij}\,\rho_\alpha\right\}, \tag{35}$$

where the discrete pressure gradient is

$$\left[\frac{\Delta p}{\Delta x}\right]_{ij} = \begin{cases}\dfrac{[\lambda]^{\mathrm{A}}_{ij}}{[\lambda]^{\mathrm{U}}_{ij}}\dfrac{p|_{\tilde{\Omega}^e}(\boldsymbol{x}_j)-p|_{\tilde{\Omega}^e}(\boldsymbol{x}_i)}{|\boldsymbol{x}_j-\boldsymbol{x}_i|} & \text{if}\quad \partial\Omega'_{ij}\subset\partial\Omega_l\\ \dfrac{\psi_l(\boldsymbol{x}_j)-\psi_l(\boldsymbol{x}_i)}{|\boldsymbol{x}_j-\boldsymbol{x}_i|} & \text{otherwise}\end{cases}. \tag{36}$$

2.3 Phase transport

In the transport equation, the phase velocity at the interface is evaluated as

$$[\boldsymbol{u}_\alpha]_{ij} = -[\lambda_\alpha]^{\mathrm{U}}_{ij}\,[k]^{\mathrm{H}}_{ij}\left\{\left[\frac{\Delta p}{\Delta x}\right]_{ij} - g_{ij}\rho_\alpha\right\}. \tag{37}$$

where the discrete pressure drop is given by Eq. 36. In Eq. 37, λ_α is the only function of saturation, such that the transport equation can be linearized substituting

$$\left[\lambda_\alpha\left(S^\nu_\alpha\right)\right]^{\mathrm{U}}_{ij} \approx \left[\lambda_\alpha\left(S^{\nu-1}_\alpha\right)\right]^{\mathrm{U}}_{ij} + \left[\left.\frac{\mathrm{d}\lambda_\alpha}{\mathrm{d}S_\alpha}\right|_{S_\alpha=S^{\nu-1}_\alpha}\left(S^\nu_\alpha - S^{\nu-1}_\alpha\right)\right]^{\mathrm{U}}_{ij}, \tag{38}$$

where $[\ ]^U_{ij}$ denotes the usual phase-by-phase upwinding (see Eq. 32).

References

1. Aarnes, J.: On the use of a mixed multiscale finite elements method for greater flexibility and increased speed or improved accuracy in reservoir simulation. Multiscale Model. Simul. **2**(3), 421–439 (2004)
2. Aarnes, J., Kippe, V., Lie, K.: Mixed multiscale finite elements and streamline methods for reservoir simulation of large geomodel. Adv. Water Resour. **28**, 257–271 (2005)
3. Arbogast, T.: Numerical subgrid upscaling of two phase flow in porous media. Tech. Rep., Texas Institute for Computational and Applied Mathematics, The University of Texas at Austin (1999)

4. Arbogast, T.: Implementation of a locally conservative numerical subgrid upscaling scheme for two phase darcy flow. Comput. Geosci. **6**, 453–481 (2002)
5. Arbogast, T., Bryant, S.L.: Numerical subgrid upscaling for waterflood simulations. SPE 66375, presented at the SPE Symp on Reservoir Simulation, Houston, 11–14 February (2001)
6. Chen, Z., Hou, T.Y.: A mixed finite element method for elliptic problems with rapidly oscillating coefficients. Math. Comput. **72**(242), 541–576 (2003)
7. Christie, M.A., Blunt, M.J.: Tenth SPE comparative solution project: a comparision of upscaling techniques. SPE 66599, presented at the SPE Symp on Reservoir Simulation, Houston, 11–14 February (2001)
8. Hou, T.Y., Wu, X.H.: A multiscale finite element method for elliptic problems in composite materials and porous media. J. Comp. Phys. **134**(1), 169–189 (1997)
9. Jenny, P., Lee, S.H., Tchelepi, H.: Multi-scale finite-volume method for elliptic problems in subsurface flow simulation. J. Comp. Phys. **187**(1), 47–67 (2003)
10. Jenny, P., Lee, S.H., Tchelepi, H.: Adaptive multiscale finite-volume method for multi-phase flow and transport in porous media. Multiscale Model. Simul. **3**(1), 50–64 (2004)
11. Jenny, P., Lee, S.H., Tchelepi, H.: Adaptive fully implicit multi-scale finite-volume method for multi-phase flow and transport in heterogeneous porous media. J. Comp. Phys. **217**, 627–641 (2006)
12. Lunati, I., Jenny, P.: Multi-scale finite-volume method for compressible flow in porous media. J. Comp. Phys. **216**, 616–636 (2006)
13. Lunati, I., Jenny, P.: Treating highly anisotropic subsurface flow with the multiscale finite-volume method. Multiscale Model. Simul. **6**(1), 208–218 (2007)
14. Renard, P., de Marsiliy, G.: Calculating equivalent permeability: a review. Water Resour. Res. **20**(5-6), 253–278 (1997)
15. Wolfsteiner, C., Lee, S.H., Tchelepi, H.A.: Well modeling in the multiscale finite volume method for subsurface flow simulation. Multiscale Model. Simul. **5**(3), 616–636 (2006)